Title

Sex- and GABAergic-modulated neuronal subnetwork assemblies in the developing somatosensory cortex

Jui-Yen Huang[1-3*], Michael Hess[3#], Abhinav Bajpai[4], Scott J Barton[1,3], Xuan Li[1-2], Liam N Hobson[1-2], Hui-Chen Lu[1-3*]

[1]Department of Psychological and Brain Sciences, Indiana University, Bloomington, IN 47405.

[2]Program in Neuroscience, Indiana University, Bloomington, IN 47405.

[3]The Linda and Jack Gill Center for Biomolecular Sciences, Indiana University, Bloomington, IN 47405.

[4]Research Technologies, Indiana University Bloomington, IN 47408.

[#]Current address: Neuroscience Graduate Program, Emory University, Atlanta 30322

Corresponding Author and Address:

Hui-Chen Lu, Ph.D.

Gill Center and Department of Psychological and Brain Sciences

Indiana University

1101 E. 10th Street

Bloomington, IN 47405

Tel: 812-856-4998

Fax: 812-856-7187

Email: hclu@indiana.edu

Jui-Yen Huang, Ph.D.

Gill Center and Department of Psychological and Brain Sciences

Indiana University

1101 E. 10th Street

Bloomington, IN 47405

Tel: 812-856-5869

Fax: 812-856-7187

Email: juiyhuan@indiana.edu

Summary

Neuronal subnetworks are common features of adult cortical circuits and serve as functional units for information processing and encoding. To determine when neuronal subnetworks are established, we employed *in vivo* calcium imaging to monitor neuronal activity in the primary somatosensory cortex (S1) of awake mice during early postnatal development. We found several striking developmental trajectories: (1) neuronal activity frequencies and network synchrony were sex-dependent; (2) neuronal subnetworks merged as early as P11; (3) the number of neurons in a subnetwork decreases with increasing age; (4) subnetwork neurons are initially spatially segregated, but become intermingled with other subnetworks neurons with increasing age; (5) neurons within the same subnetwork acquire a more cohesive activity pattern as age increases, and (6) enhancing GABAergic activity at P15 acutely increased female but not male subnetwork coherence. Together, our findings demonstrate that P11-P21 is the critical time for subnetwork assembly and GABAergic inputs strengthen subnetwork coherence.

Keywords

Neuronal subnetwork, clustering, spontaneous calcium activity, cortical development, GABAergic neurons, sensory processing.

Introduction

Neuronal subnetworks have been identified as groups of neurons that have similar receptive fields, respond to a similar type of stimulation, or exhibit increased connectivity relative to the whole network (Cossell et al., 2015; Lee et al., 2016; Peron et al., 2015; Yassin et al., 2010; Yoshimura et al., 2005). In mature cortical circuits, neurons from different subnetworks encoding different information are spatially intermingled over large brain volumes (Cossell et al., 2015; Lee et al., 2016; Peron et al., 2015). Despite anatomical separation, neurons from the same subnetwork co-activate as functional assemblies and generate spontaneous activity patterns that resemble externally-evoked activity patterns even when receiving minimal external input (Buzsaki, 2010; Carrillo-Reid et al., 2016; Harris and Mrsic-Flogel, 2013; Malvache et al., 2016; Miller et al., 2014; Peron et al., 2020). However, little is known about when these functional subnetworks are formed and what are the underlying mechanisms for subnetwork assembly.

Two-photon calcium imaging of awake behaving pups has been utilized to visualize neuronal activity in the developing brain. These studies revealed that calcium events in both glutamatergic and GABAergic neurons are highly correlated and synchronized in the first postnatal week (Golshani et al., 2009; Goncalves et al., 2013; He et al., 2018; Mizuno et al., 2018; Modol et al., 2020; Nakazawa et al., 2020). In the primary somatosensory cortex (S1), three distinct early developmental phases of neuronal network properties have been described for layer 4 (L4, the layer receiving sensory input): patchwork-type (P1-P7), synchronized (P7-P10/11), and sparse (P11/P12) (Mizuno *et al.*, 2018; Nakazawa *et al.*, 2020). However, the developmental trajectory of L4 neuronal subnetworks after P11 remains elusive. What is known is that L2/3 neuronal activity pattern from P11 to P21 transitions from highly correlated and synchronous to sparse (Golshani *et al.*, 2009; He *et al.*, 2018; van der Bourg et al., 2017). This transition in neuronal network activity coincides with the maturation of recurrent excitatory and inhibitory circuits in developing S1 (Ashby and Isaac, 2011; Daw et al., 2007; Gour et al., 2021; Itami et al., 2007; Kalemaki et al., 2022; Valiullina et al., 2016). Yet, the impact of the maturing GABAergic inputs on functional properties of developing cortical subnetworks has not been investigated.

To determine when cortical neurons begin to assemble into functional subnetworks, we conducted two-photon calcium imaging to monitor the activity of L2-4 S1 neurons during the 2nd ~ 3rd postnatal weeks and examined if the maturation of GABAergic inputs modulates subnetwork function. We observed sex-dependent developmental trajectories of neural network activity. Using statistically grounded approaches and data-driven clustering algorithms, such as k-means clustering and Louvain

community detection algorithms, we were able to reveal functional neuronal subnetworks at P11, the earliest age we imaged. However, the similarity in the activity patterns among neurons in the same subnetwork increases with age, and the increase in trajectory was faster in males than females. We found acutely enhancing GABAergic activity in female mice at P15 significantly increased the subnetwork coherence in S1 L2-4 neurons. Taken together, we showed the early assembly of S1 neuronal subnetworks and provided supportive evidence that GABAergic inputs contribute to the establishment of coherent subnetworks.

Results

A sex difference in the calcium event frequency and activity correlation within neuronal pairs in the developing S1

To assess how S1 neurons assemble their network activity during development, we performed *in vivo* two-photon calcium imaging using the red calcium sensor jRGECO1a to monitor neuronal activity in head-restrained and awake animals. We injected AAV carrying jRGECO1a into S1 via stereotaxic intracranial injections at P1~2 and installed cranial window at P8-P9 (Figure 1A, Figure S1). The window cleared within two days after the installation and remained clear until P21 (Figure 1B upper panel). *In vivo* two-photon calcium imaging with awake behaving pups in a head-restrained configuration was performed at P11, 13, 15, 18, and 21 (STAR Methods; Figure 1A, Figure S1A-C). A field of 505 x 505 μm was imaged sequentially at different cortical depths below the surface to include S1 L2/3 and L4 (STAR Methods), and the same imaged areas were tracked and imaged over multiple days. To reveal the default organization of cortical network activity, minimizing body movement-derived brain activity was crucial. Thus, body and facial movements were recorded simultaneously during calcium imaging (Figure S1C). This allowed us to isolate periods when pups had minimal body movement, identified as stationary status, for the following data analysis (STAR Methods; Figure S1F, G).

We found a significant developmental decline of calcium event frequencies from P11 to P15 (Figure 1C, D). Unexpectedly, we also observed that female S1 neurons exhibited significant higher frequency of calcium events compared to males at all ages (Figure 1D). Such increases are unlikely to result from higher calcium amplitudes because the accumulated area of calcium events is lower in female neurons (Figure S1H). To quantify the calcium event relationship between neuronal pairs, we first computed the Pearson correlation coefficient of all neuronal pairs (Figure 1E). We found interesting

dynamic changes during P11-P21: the mean correlation coefficients of all neuronal pairs first significantly decreased from P11 to P15 in both females and males and then increased at P18 (Figure 1F). To elucidate if anatomical distance between neuronal pairs affects their calcium event correlations, we also plotted the correlation coefficients against the inter-neuronal distance. We found that the correlation coefficients of neuronal pairs with inter-neuronal distances between 0-400 µm were significantly reduced from P11-P15 in both females and males (Figure 1G). We also found that females had a significantly greater correlation coefficient versus the inter-neuronal distance at P11 and P15 (Figure 1G), but the difference was less at P21 (Figure 1H).

To investigate activity patterns from grouped neurons, we quantified the occurrence of peaks of synchrony (synchrony frequency), defined as network events with a significantly higher proportion of neurons participating (Figure 1I, STAR Methods). Results showed that the synchrony frequency significantly decreased with age in both sexes (Figure 1J) and was significantly larger in females (Figure 1J). The proportion of neurons participating in peaks of synchrony gradually decreased from P11-P18 in both sexes (Figure 1K). Moreover, females had a significantly larger proportion of neurons activated in peaks of synchrony at P11, P13, and P21 compared to males (Figure 1K).

These results showed that the spontaneous neuronal activity gradually decreased, de-correlated, and desynchronized in both L2/3 and L4 with age. Here we report for the first time that females have significantly higher calcium event frequency and activity correlation than males.

The properties of the S1 cortical neuronal subnetwork from 2nd to 3rd postnatal weeks

Given that calcium events were gradually desynchronized and de-correlated from P11-P21, we next asked if the developmental decorrelation and desynchronization allowed neurons to preferentially assemble into the subnetworks. To detect and sort calcium events with similar activity patterns, we employed an unsupervised k-means clustering algorithm (Malvache *et al.*, 2016; Modol *et al.*, 2020) to cluster covariance matrix generated by frame-by-frame calcium events (STAR Methods; Figure 2A-C). This was followed by assigning neurons to the calcium event cluster that they maximally contributed to, and subsequently reveal the neuronal subnetwork (STAR Methods; Figure 2D). The silhouette value is a measure of how similar a point to its own cluster (cohesion) compared to other clusters (separation). First, we inspected the silhouette value that represented the cluster's similarity degree to evaluate the coherence of calcium event clusters. We found that the silhouette value significantly increased from P11

to P21 in both sexes (Figure 2E). Notably, the males had significantly higher silhouette values than females across all ages (Figure 2E). After assigning neurons to the calcium event clusters in which they maximally participated (STAR methods), we found that neuronal subnetworks were already present at P11, and their number was relatively consistent across development, except for a transient increase at P15 in females (Figure 2F).

To determine subnetwork configuration stability, we categorized neurons according to whether or not they participated in the calcium event cluster. If they participated in the cluster, we asked if they solely participated in just one or multiple clusters. With these characteristics, neurons were separated into the following three categories: non-cluster neurons, single-cluster neurons, and multiple-cluster neurons. We found that the percentage of non-cluster neurons increased with age (Figure 2G), with a concomitant decrease in the percentage of single-cluster neurons (Figure 2H). The percentages of multiple-cluster neurons stayed similar from P11-P21 (Figure 2I). To test the robustness of the clustering, we also performed k-means clustering by using different similarity matrices such as cosine similarity, Jaccard similarity, as well as the Louvain community detection algorithm (STAR methods). Importantly, each of the additional four clustering methods revealed very similar developmental trajectories: developmental increases in silhouette values, augmentation of the percentage of non-cluster neurons, and a reduction in the percentage of single-cluster neurons (Figure S2B).

The age-dependent increase of silhouette values (Figure 2E) suggests that the recurrent neuronal activity patterns may become stronger within the same cluster or more discrete to other clusters as S1 matures. To evaluate this further , we computed the tetrachoric correlation coefficient, which is akin to the Pearson correlation coefficient but more appropriate for binary data (Dorn and Ringach, 2003) for all neuronal pairs and all neuronal pairs within their specific subnetwork. We found the mean tetrachoric correlation coefficients from all neuronal pairs significantly decreased from P11-P15 in both sexes and then increased at P18 (Figure 2J, Figure S2C). On the other hand, the mean tetrachoric correlation coefficients of neuronal pairs within the same cluster continuously increased from P11-P21 regardless of sex (Figure 2K). However, males had significant higher correlations than females (Figure 2K). Notably, tetrachoric correlation coefficients of neuronal pairs within the same cluster were higher (Figure 2K) compared to the value from all neuronal pairs (Figure 2J).

Previous studies demonstrate that neurons within the same subnetwork are spatially intermingled and distributed over large brain volumes in adult mice (Cossell *et al.*, 2015; Lee *et al.*, 2016; Peron *et al*., 2015). Thus, we also examined the topographical distribution of each neuron according to

their subnetwork identification (Figure 2L). We calculated the distance of each neuronal pair within the same cluster (data not shown) and the distance of each neuron to its cluster centroid as indices for the physical size of the neuronal subnetwork. We found no significant change in the physical size indices from P11-P21 regardless of sex (Figure 2M). Interestingly, the pairwise distance of cluster centroids significantly decreased in both sexes (Figure 2N). The results suggested that the spatial distribution of neurons within the same subnetwork defined by similar activity patterning were segregated according to their subnetwork at P11, and then gradually became spatially intermingled with neurons in other subnetworks by P21 (Figure 2N).

Taken together, our results reveal that neuronal subnetworks are present as early as P11. However, subnetwork properties dynamically change from P11-P21. Despite fewer neurons participating in single or multiple clusters with increasing age, the coherence (silhouette values of calcium event clusters) of the calcium event activity patterns increased significantly from P11-P21. Our finding identifies that the 2nd and 3rd postnatal weeks are a critical period for S1 neurons to refine their functional connections to form highly correlated neuronal subnetworks that are independent from other subnetworks.

Enhancing GABAergic transmission facilitates the cohesiveness of female neuronal subnetworks

The number of GABAergic synapses onto the soma of L4 glutamatergic neurons gradually increases from P9 - P28 (Gour *et al.*, 2021). In agreement with anatomical observations, the frequency of sIPSCs onto L2/3 excitatory neurons increases from P10-P20 (Kalemaki *et al.*, 2022). To test the hypothesis that the developmental maturation of GABAergic inputs contributed to neuronal subnetwork establishment, we employed a designer receptor exclusively activated by designer drugs (DREADD)-based approach to acutely enhance GABAergic neuronal transmission (Alexander et al., 2009; Dimidschstein et al., 2016). Specifically, we injected an AAV mixture of synapsin-jRGECO1a and Dlx5/6-hM3Dq at P1~2 and installed cranial windows at P8~P9 (Figure 3A). We confirmed that the majority of jRGECO1a expressing neurons are glutamatergic neurons and that Dlx5/6-hM3Dq positive neurons are mainly GABAergic (Figure S3) as previously reported (Dimidschstein *et al.*, 2016). We chose to determine the impact of GABAergic inputs on the neuronal subnetwork at P15 because this is the age when the silhouette values differed most between males and females (Figure 2E) and is also the midpoint of the transitions for the various developmental trajectories identified above. After baseline calcium imagining

at P15, hM3Dq ligand, clozapine-N-oxide (CNO; 5 mg/Kg, intraperitoneally) were injected into pups to enhance GABAergic activity (Figure 3A). Thirty to sixty minutes after CNO treatment, we conducted calcium imaging. CNO treatment significantly reduced calcium event frequency in females but not males (Figure 3B). In grouped neuronal activity, we found that CNO treatment significantly decreased synchrony frequency in females (Figure 3C). Furthermore, cluster analysis showed that CNO treatment significantly increased the silhouette values of calcium event clusters in females (Figure 3D). However, CNO had no impact on the number of subnetworks (Figure 3E), percentage of non-cluster neurons (Figure 3F), or percentage of single-cluster neurons (Figure 3G). Interestingly, CNO significantly increased the percentage of multiple-cluster neurons (Figure 3H). Moreover, the mean tetrachoric correlation coefficient of all neuronal pairs was not significantly altered by CNO (Figure 3I), but the mean tetrachoric correlation coefficient within the same cluster was significantly increased by CNO (Figure 3J). CNO treatment did not change the distance of neurons to the subnetwork centroid (Figure 3K) or the pairwise distance of cluster centroids (Figure 3L). Taken together, our results suggest that acutely increasing GABAergic neuronal excitability is sufficient to enhance subnetwork coherence in females.

Discussion

We characterized the developmental profile of S1 L2/3 and L4 neuronal calcium events in female and male mouse pups from P11-P21. We initially analyzed by cortical layer (L2/3 and L4), age, and sex and found that calcium event networks were very similar between L2/3 and L4 (Figure S1I-J, S2A-D). Thus, data from L2/3 and L4 were merged and further analyzed with two-way ANOVA to examine the effect of age and sex. Our data show for the first time that neuronal subnetworks in mouse S1 at P11. Nascent subnetworks are then refined and mature from P11 to P21 in a sex-dependent manner. Acute strengthening of GABAergic inputs at P15 increased cohesiveness among neurons within female subnetworks.

Developmental sparsification, decorrelation, and desynchronization of spontaneous activity during the 2nd~3rd postnatal week

The sparsification of spontaneous activity in the 2nd ~3rd postnatal weeks we observed in both S1 L2/3 and L4 agree with previous findings (Golshani *et al.*, 2009; He *et al.*, 2018; Sigalas et al., 2017; van der Bourg *et al.*, 2017). In addition to the developmental changes, we also observed that females had

heightened calcium event frequency, paired correlated activity, and synchrony activity (Figure 1) from P11-P21. By recording local field potentials in acute brain slices of male and female mice, Sigalas et al. (2017) also showed that female mice had significantly longer and a greater frequency of up-state activity, a type of synchronous network activity exhibited during quiet wakefulness (Haider et al., 2006; Shu et al., 2003), compared to aged-matched male mice from P17-P20. Our finding that the enhancement of GABAergic neuronal activity at P15 acutely decreased calcium event frequency in females suggests (Figure 3B) that the maturation of GABAergic inputs is involved in developmental sparsification, at least in females. The unexpected sex-difference phenomenon we observed suggests that other underlying mechanisms also regulate the phenomenon during cortical development. One possible contribution to this could lie with astrocytes. Increasing astrocytes calcium dynamics induced long-lasting synaptic potentiation in the hippocampus (Gerasimov et al., 2021; Van Den Herrewegen et al., 2021). Astrocytes interact with neurons via their fine processes, which are developing from P7-P21 in S1 as well (Clavreul et al., 2019; Stogsdill et al., 2017). Interestingly, astrocyte-specific translatomic analysis showed that male astrocytes mature faster at the molecular signature levels than females (Rurak et al., 2022). If astrocytes underlie the sex differences in calcium dynamics should be examined with future studies.

The 2nd and 3rd postnatal weeks are a critical time for cortical subnetwork functional maturation

We utilized k-means clustering and Louvain community detection algorithms to reveal neuronal subnetworks, defined as clustering of recurrent activity patterns occurring upon spontaneous activity. The neuronal subnetwork emerged as early as P11 when the neurons within the same subnetwork are more spatially segregated. From P11-P21, the nascent subnetworks undergo configuration re-arrangement (participating in single/multiple calcium event cluster(s) or not participating in any cluster). By P21, the neuronal subnetwork is refined as a unit with a higher correlated activity pattern while its spatial distribution is widely intermingled. In our study, most imaged neurons (~90%) are glutamatergic neurons, and ~10% neurons are GABAergic neurons (Figure S3E), and both excitatory and inhibitory neurons participate into the subnetwork assembly. A recent study shows that touch or voluntary whisker movement activate different subsets of inhibitory neurons-fast-spiking or vasoactive intestinal polypeptide-expressing interneuron, respectively (Yu et al., 2019). These findings indicate that neuronal computation involves the recruitment of diverse types of GABAergic neurons to integrate with excitatory neurons into precisely structured circuits. Future studies will be needed to determine when and each subtype of GABAergic neuron engage neuronal subnetwork to assist cortical microcircuits

computation. In addition, detailed sensorimotor developmental analysis has shown that mice commence bilateral whisking at P10 and exploring the environment with their whiskers at P11 (Arakawa and Erzurumlu, 2015; van der Bourg *et al.*, 2017). Thus, it will be important to determine how experience-dependent mechanisms modulate neuronal subnetwork assembly.

During early cortical sensory map development, spontaneous and often synchronized neuronal activity guides circuit formation and refinement, such as spontaneous waves of activities in visual pathways and patch-like activity in the whisker-barrel pathway (Mizuno *et al.*, 2018; Thompson et al., 2017). After the initial formation of sensory maps, neuronal activity patterns transit to those with sparse coding features and form subnetwork units, which would be efficient for sensory coding from a computational perspective (Avitan and Stringer, 2022). In other words, aberrant spontaneous activity patterns would interfere with information coding of the surrounding environment and disrupt appropriate sensory processing (Ferezou and Deneux, 2017; Hartmann et al., 2015; Karvat et al., 2021). Future studies will be needed to determine the functional significance of sex differences in developmental programs and their impact on neuronal network development and behavior, in both normal and pathological conditions.

Figure legend

Figure 1. A sex difference in the calcium event frequency and activity correlation within neuronal pairs in the developing S1. (A) The illustration shows the experimental timeline. Mice were injected with AAV-carrying jRGECO1a (AAV9-Syn.NES-jRGECO1a) at P1~2 followed by cranial window installation at P8~9. (B) Upper panel: The cranial window implanted at P9 remains optically transparent during the investigation. Lower panel: A superficial image showing the vasculature pattern under the two-photon microscope. A, anterior; P, posterior; M, midline; L, lateral. (C) Exemplar raster maps from female and male mice at P11 (female 160 cells; male 122 cells) and P21 (female 197 cells; male 163 cells). (D) Violin plot showing the distribution of event frequency from every female (F) and male (M) neuron. Kruskal-Wallis test. ns, no significant; *p<0.05; ***p< 0.001. (E) Exemplar correlation matrices displaying the correlation coefficients between all possible pairs of cells from a female mouse. (F) The mean correlation coefficient across developmental ages. Two-way ANOVA *post hoc* Tukey's multiple-comparisons test. **p<0.01; ****p<0.0001. (G, H) The correlation coefficients against inter-neuronal distance at P11, P15, and P21. Two-way ANOVA *post hoc* Tukey's multiple-comparisons test. ***p<0.01; **** p<0.0001. (I) The upper panel shows the raster plot of L2/3 neurons from a P11 female pup. The lower panel shows the cumulative fraction of active neurons over time in the upper panel. The fraction of recruited neurons above the threshold was identified as one synchronous event. (J) The synchrony frequency. Two-way ANOVA main effect. ****p<0.0001 for sex or age. (K) The fraction of active neurons at the maximum point of each synchronous burst. Kruskal-Wallis test. ns, no significant; ****p<0.0001. The number of mice in different age groups. P11: 10F, 16M; P13: 9F, 14M; P15: 8F, 14M; P18; 2F, 9M; P21: 3F, 10M

Figure 2. The properties of the S1 cortical neuronal subnetwork from 2nd to 3rd postnatal weeks. (A) Raster plot of detected calcium events from a 30-second time interval during stationary status. (B) The covariance similarity matrix generated by calcium event (frame-frame) in A. (C) The re-sorted covariance similarity matrix according to unsupervised k-means clustering algorithm. Seven calcium event clusters were identified in this dataset. About 160 frames were unable to be clustered due to the sparseness of neuronal activity. (D) The re-sorted raster map according to neuronal subnetwork (y-axis) and calcium event cluster (x-axis). After assigning neurons to the calcium event clusters in which they participated the most, there are five neuronal subnetworks (color coded). Calcium event clusters lacking significantly neuronal participation were removed and not shown. (E) The silhouette value of calcium event clusters. (F) The number of neuronal subnetworks. (G) The percentage of neurons not participating in any calcium

event cluster. (H) Percentage of neurons participating in single calcium event cluster. (I) Percentage of neurons participating in multiple calcium event clusters. (J) The tetrachoric correlation coefficient from all neuronal pairs. (K) The tetrachoric correlation coefficient from neuronal pairs within the same subnetwork. Two-way ANOVA main effect. *p<0.01; **p<0.01; ****p<0.0001 for sex or age. Two-way ANOVA *post hoc* Tukey's multiple-comparisons test. #<0.05; ##p<0.01; ##p<0.001, ####p<0.0001 for male (blue) or female (red). (L) The neuronal topography map. Empty circles indicate cells not participating in any calcium event cluster. Filled colored circles indicate different neuronal subnetworks. (M) The mean distance of neuron to the subnetwork centroid. Individual data points represent the mean distance from one neuronal subnetwork. (N) The mean distance of subnetwork centroid. Individual data points represent the distance of subnetwork centroid pairs. Kruskal-Wallis test. **p<0.01; ****p<0.0001. Animal numbers are the same as in Figure 1.

Figure 3. Enhancing GABAergic transmission facilitated the functional assembly of neuronal subnetwork. (A) Illustration showing the experimental design. The mouse was injected with AAV-carrying jRGECO1a (AAV9-Syn.NES-jRGECO1a) and excitatory DREADD (AAV9-hDlx-hM3Dq-P2A-nuclear dTomato) at P1~2 followed by cranial window installation at P8~9. At P15, pups were imaged before CNO administration. After imaging, pups were administered CNO and imaged 30 minutes later. (B) Violin plot shows the distribution of event frequency from every neuron. Kruskal-Wallis test. ***p<0.001. The synchrony frequency (C), the silhouette value of calcium event cluster (D), number of neuronal subnetworks (E), percentage of neurons not involved in any calcium event cluster (F), percentage of neurons participating in a single cluster (G), percentage of neurons participating in multiple clusters (H), tetrachoric correlation coefficients from all neuronal pairs (I), and tetrachoric correlation coefficients from neuronal pairs within the same subnetwork (J). Individual data points and lines represent one data point before and after CNO administration. Two-way Repeat ANOVA main effects are stated in the figure. Two-way Repeat ANOVA *post hoc* Šidák's multiple-comparisons test. #p<0.05; ##p<0.01. (K) The mean distance of neuron to the subnetwork centroid. Individual data points represent the mean distance from one neuronal subnetwork. (L) The mean distance of subnetwork centroid. An individual data point represents the distance between subnetwork centroid pairs. Animal number: 4F, 4M.

Acknowledgments

This work is supported by NIH-NINDS (R01NS048884, R01NS086794), NIH-NIDA (R01DA053746), startup funds from the College of Arts and Sciences, and Gill endowment fund to Dr. Hui-Chen Lu. This work used the Extreme Science and Engineering Discovery Environment (XSEDE) (Towns et al., 2014), which is supported by National Science Foundation grant number ACI-1663578. We thank Joseph Kimmel Leffel and Bruna Baumgarten Krebs for their technical support. We thank Drs. Carlos Portea-Cailliau, Duton Oyesanmi, Ju Lu, Nathalie L. Rochefort, Ruth Eberle, and Sander W. Keemink for the coding support. We thank clinical veterinarian Randalyn Shepherd for excellent support and suggestions to keep post-surgical pups healthy. We thank Drs. Ehren Lee Newman, Zoran Tiganj, and Richard Betzel for the critical suggestions related to additional clustering analysis. We thank Eric Wernert, Esen Tuna, and James Robert McCombs for assisting with data storage and using high-performance computing resources. We also thank helpful comments from Miss Ashley Xu and Drs. Cary Lai, Ehren Lee Newman, Ken Mackie, Richard Betzel, and Simon Chen.

Author Contributions

Conceptualization: JY.H., HC.L

Experimentation/Investigation: JY.H., M.H., A.B

Data acquisition: JY.H.

Data curation: JY.H., S.J.B., X.L., LN.H.,

Methodology: JY.H., M.H., A.B., S.J.B.

Writing: JY.H., HC.L., M.H.

Funding acquisition: HC.L.

Resource: JY. H., HC.L.

Supervision: JY. H., HC.L.

Declaration of Interests

The authors declare no competing interests.

STAR Methods

Key Resources Table

Chemicals and Antibodies

REAGENT or RESOURCE	SOURCE	IDENTIFIER
Antibodies		
Mouse anti-CamK2	AbCam	Cat# ab22609; RRID: AB_447192
Rabbit-anti RFP	Rockland Antibodies	Cat# 600-401-379; RRID: AB_2209751
Chicken anti-GFP	Aves	Cat# GFP-1010; RRID: AB_2307313
Goat anti-chicken Alexa Fluor 488	ThermoFisher	Cat# A11039; RRID: AB_2534096
Goat anti-rabbit Alexa Fluor 555	ThermoFisher	Cat# A21429; RRID: AB_2535850
Goat anti-mouse Alexa Fluor 647	ThermoFisher	Cat# A21236; RRID: AB_2535805
Bacterial and virus strains		
pAAV9. Syn.NES-JRGECO1a	(Dana et al., 2016)	RRID: Addgene_100854
pAAV9.hDlx-GqDREADD-dTomato	(Dimidschstein *et al.*, 2016)	RRID: Addgene_83897
Chemicals, peptides, and recombinant proteins		
KCl	Sigma-Aldrich	Cat# P9541
Trizma-HCl	Sigma-Aldrich	Cat# T5941
Triton X-100	Sigma-Aldrich	Cat# X-100
EconoTaq Plus Green 2x mater mix	Lucigen	Cat# 30033-1
FastGreen FCF dye	Sigma-Aldrich	Cat# F7252
Glass micropipettes	Sutter Instruments	Cat # BF100-50-10
Clozapine-n-oxide	Sigma-Aldrich	Cat# C0832
Paraformaldehyde	Sigma-Aldrich	Cat# 8.18715
Ethylene glycol	Sigma-Aldrich	Cat# 324558
polyvinyl pyrrolidone	Sigma-Aldrich	Cat# PVP360
Normal goat serum	Jackson Immunoresearch	Cat# 005-00-121
DAPI	Thermo Fisher	Cat# D3571
Prolong Diamond Antifade	ThermoFisher	Cat# P36961

mounting medium		
Experimental models: Organisms/strains		
Wildtype C57/B6 mice	Jackson Laboratory	
R26-LSL-hM4Di-DREADD	Jackson Laboratory	RRID: IMSR_JAX:026219
R26-LSL-Gq-DREADD mice	Jackson Laboratory	RRID: IMSR_JAX:026220
GAD67-GFP	(Tamamaki et al., 2003)	
Software and algorithms		
NIS Element	NIKON microscope	https://www.microscope.healthcare.nikon.com/
Python 3	Python Software Foundation	https://www.python.org/
Adobe Illustrator	Adobe	https://www.adobe.com/ca/products/ illustrator.html
MATLAB2022a	Mathworks	https://www.mathworks.com/products/matlab.html
FIJI	(Schindelin et al., 2012)	https://imagej.net/software/fiji/
Suite2p	(Pachitariu et al., 2017)	http://www.suite2p.org
FISSA	(Keemink et al., 2018)	
DeepLabCut	(Mathis et al., 2018)	
Facemap	(Stringer et al., 2019)	
Prism 9	GraphPad	https://www.graphpad.com/scientificsoftware/prism/

RESOURCE AVAILABILITY

Lead contact

Further information and requests for resources and reagents should be direct to and will be fulfilled by the Lead Contact Jui-Yen Huang (juiyhuan@iu.edu) and Hui-Chen Lu (hclu@indiana.edu)

Materials availability

This study did not generate any unique reagents.

Data and code availability

- All data reported in this paper were uploaded to DataJoint company (https://www.datajoint.com/) will be shared by the lead contact upon request.
- Any additional information required to reanalyze the data reported in this paper is available from the lead contact upon request.

EXPERIMENTAL MODEL AND SUBJECT DETAILS

Some animals in figures 1 and 2 are mixed C57/B6J with R26-LSL-hM4Di-DREADD or R26-LSL-Gq-DREADD mice. All animals in figure 3 were C57/B6J mice. Both male and female mice were used for data analysis. All procedures involving animals were performed in accordance with the Indiana University Bloomington Animal Research Committee, and the NIH Guide for the Care and Use of Laboratory Animals.

METHOD DETAILS

P1/P2 injection of AAV for jRGECO1a expression.

The surgical procedure was conducted as described previously (He *et al.*, 2018) with slight modification. pAAV9. Syn.NES-JRGECO1a(100854-AAV9), pAAV9.hDlx-GqDREADD-dTomato (83897-AAV9), and pAAV9.hDlx-GiDREADD-dTomato (83896-AAV9) viruses were purchased from Addgene and diluted to a working titer of $1x10^{13}$ GC/ml with 0.05% FastGreen FCF dye. Postnatal one- or two-day male and female pups were anesthetized with isoflurane (5% for induction, 2-3% maintenance via a nose cone, vol/vol). Subcutaneous injection of ketofen (5mg/Kg) was administered. The surgical region was disinfected with 4% chlorhexidine and 70% alcohol. We used soft silicone ear bars to position the mouse on the stereotaxic frame to make the desired injection area (presumptive somatosensory cortex) as flat as possible. We used scissors to create a 3-4 mm triangular skin flap over S1. The periosteum was gently cleared under the skin flap using a sterile Q-tip. The skin flap (folded back) was covered with a piece of saline-soaked Gelfoam to prevent the skin from drying during the procedure. At the injection site, the

bone was drilled lightly to create a small crack, permitting injection via pulled-glass capillary without exposing the dura. Glass micropipettes (O.D. 1 mm, I.D. 0.5 mm Sutter Instruments, cat no. BF100-50-10) pulled by using a P1000 pipette puller (Shutter Instruments, CA, USA) were used to inject ~200 nL of AAV into the superficial cortex, using an injection pump equipped with a Hamilton syringe. The pipettes were positioned for injection at 70~90^0 angle to the skull surface and gently pierced through the cracked bone and into the superficial cortex. The injection flow rate was 50 nL/min. The light blue dye was visible on the brain surface of pups with successful injection. The glass pipettes were left in place for one minute before withdrawing the pipette. The skin flap was sealed with a small drop of VetBond to the injection site. The entire surgery was complete in 10-15 min per pup. The pups recovered on a warm blanket before being returned to the dam.

Cranial window surgery

The surgical procedure was conducted as described previously (He *et al.*, 2018) with slight modification. Mice aged at P8~ 9 were anesthetized with 5% isoflurane for induction, followed by 2-3% maintenance (vol/vol, via nosecone). Pups also received Ketoprofen (5 mg/Kg, s.c.) and Dexamethasone (1 mg/Kg, s.c.) and a mixture of lidocaine + epinephrine (4 mg/Kg and 0.1 mg/Kg, topical, surgical region) for analgesia and anti-inflammatory purposes. Pups were positioned by using blunt ear bars on the stereotaxic frame. The original AAV injection site was apparent as a well-healed triangular scar on the skin. The pup's head was swabbed with 4% chlorhexidine and 70% alcohol to disinfect the skin. The skin on the top of the surgical area was removed. We used a dental drill to carve a circular craniotomy, 3 mm in diameter. The drilling procedure was stopped until the bone was cracked all around the perimeter of the craniotomy. Any blood was removed immediately because an accumulation blood can make the window blurry. The entire drilled area was soaked with sterile saline using Gelfoam for at least 3 min to soften the bone. The bone fraction was gently removed and a 3 mm glass plug coverslip (generated by adhering another 2.3 mm coverslip with transparent UV-activated adhesive) was positioned over the craniotomy. The glass was sealed using cyanoacrylate then dental acrylic (Metabond). A custom-made circular head plate (less than 0.5 g, Figure S1A) was positioned over the area, centered around the cranial window, and was adhered to the skull using dental acrylic (Metabond). The pup was then placed on a heating pad with bedding for recovery and then returned to the dam when free moving. Post-surgical pups were fed with kitten-replaced milk (every 4-5 hours during daytime) to provide nutrition if pups did not gain body weight and had no milk spot in the belly. Pups became more active in seeking the dam for milk 2 days after the surgical procedure. Pups were subjected to habituation on the imaging station for 15 minutes

on the next day after surgery. After that, pups were habituated on the imaging station for 30 minutes (the average imaging time) or subjected to the imaging procedure daily.

In vivo calcium imaging in head-restrained neonatal pup

In vivo calcium imaging was performed under an unanesthetized condition. Before imaging, a metal bar was attached to the headframe (Figure S1B) to provide the anchoring point to the imaging station (Figure S1C). Calcium imaging was performed on a Nikon A1R MP$^+$ multiphoton microscope, with an Insight DeepSee infrared pulsed laser (Spectra-Physics Inc, Santa Clara, USA), resonant scanner, a 25x, 1.1 NA water immersion lens (Nikon, Japan), and Nikon Elements software. The homemade imaging station was equipped with a lightweight foam disc covered by a circular paper drape. The center of the discs was fixed so that pups could choose to rest, whisk, or walk with minimal friction. To maintain the body temperature of neonatal pups, a heating pad was placed under the imaging platform. The light source was an insight running at 1040 nm for jRGECO1a. Whole field images were acquired at 65.6 ms/frame (~15.23 Hz) (512x512 pixels). The pups' body movements were simultaneously monitored and recorded during imaging using an infrared camera (30 Hz, 1920x 1080 pixels) with 850 nm IR LED light source and IR-cut filter at 850 nm. Before calcium imaging, pups were habituated on the imaging station for at least 10 mins. To find the same field of view to image in subsequent imaging procedures, we used a vasculature map to locate landmark of the previous imaging position (Figure 1B). First, the global vasculature pattern in the cranial window was imaged by using a dissecting microscope. The location where calcium imaging was performed was marked on the map. Next, the pial surface of the vasculature pattern was also imaged under a multiphoton microscope and used as the second landmark. The whole imaging section was conducted within one hour for each animal to minimize aversive effect from maternal separation. For L2/3 imaging, the imaging location was 120-150 µm below the pia surface. For L4 imaging, the imaging location was 200-350 µm below the pia surface.

Data analysis for calcium imaging

The preprocessing of all raw calcium movie data was done using a Suites2P toolbox (Pachitariu *et al.*, 2017; Stringer *et al.*, 2019). Briefly, Suite2p first aligned all frames of a calcium movie using two-dimensional rigid registration based on regularized phase correlation, subpixel interpolation, and kriging. Suite2p computed a low-dimensional decomposition of the data, which was used to run a clustering algorithm that finds regions of interest (ROIs) based on the correlation of the pixels inside them. We inspected every ROI using the following criteria: (1) the classical morphology should be a donut-shaped

circle; (2) the neurons with obvious nuclear signals were excluded, as were cells from animals injected with pAAV9-hDlx-GqDREADD-dTomato expressed nuclear Tomato fluorescent protein (Figure S4A); (3) each ROI was never overlapping. For the neuropil correction, we used the Fast Imaging Signal Separation Analysis (FISSA) toolbox (Keemink *et al.*, 2018). The coordinates of selected ROIs and post-motion-corrected tiff files were imported to the FISSA toolbox for neuropil decontamination. After neuropil correction, the ΔF/F was calculated as $(F-F_0)/F_0$. Where the F is the extracted fluorescence signal, and F_0 is the median of the bottom 10th percentile of the fluorescent trace. To normalize the differential fluorescent change caused by the expressed jRGECO1a level in each neuron, we further calculated the modified Z score for each neuron (Goel et al., 2018; He et al., 2017). $Z\ score = \frac{F(t)-mean(baseline)}{std(baseline)}$, where the baseline period is the 10-s period with the lowest variation (s.t.d.) in ΔF/F. We used the Peakfinder function in MatLab to find the conceivable calcium transient. The actual calcium event is defined as the fluorescent peak amplitude greater than four times the noise level. The noise level is the mean Z score within five second-time windows when it has the lowest root mean square. To analyze the spontaneous calcium activity, we used the DeepLabCut toolbox (Mathis *et al.*, 2018; Nath et al., 2019) to annotate the movement of the limbs and identify the time windows when pups show minimum activity (stationary condition). In addition, the video-recorded facial movements were analyzed by Facemap Python package (Stringer *et al.*, 2019). Both annotations were plotted to visualize the overall movement of the body and whisker (Figure S1F, G). For spontaneous activity quantification, the time period with minimum body movement and whiskering was used for calculating various parameters.

For the pairwise correlation analysis, we computed the Pearson correlation coefficients for Z-score normalized traces. The correlation coefficient of each neuronal pair was further binned (25 µm/bin) based on the distance between neuronal pairs. The synchrony analysis was performed as described previously (Goncalves *et al.*, 2013). To calculate the synchrony, we reconstructed activity histograms that plotted the percent of active cells for each frame. The threshold for detecting a network event was set by repeatedly shuffling each deconvolved somatic calcium trace 100 times while maintaining the average firing rate for each cell. A surrogate activity histogram was constructed from each reshuffled trial. The threshold was calculated by first finding the peak percentage of cells active in each reshuffled trial, and then sorting these values to find the 95th percentile, which was set as the threshold for significance (p=0.05). The time point when the percent of active neurons exceeded this threshold was set as the start of an event. The time point when the percentage of active neurons fell below this level

was set as the end of the event. The mean frequency of peaks of synchrony and the mean fraction of active cells at the maximum point of each peak of synchrony were calculated.

To identify the neuronal subnetwork, we employed a similar strategy was performed as previously described (Malvache *et al.*, 2016; Modol *et al.*, 2020). The initial calcium event clusters were identified using a clustering algorithm based on calcium dynamic similarity. Unsupervised clustering of calcium events was obtained by running the k-means algorithm on the normalized covariance matrix (frame-frame) with cluster numbers ranging from 2-19. One hundred iterations of k-means were run for each cluster number, and the iteration that resulted in the best-average silhouette value was kept. Each cluster was then associated to a cell assembly that comprised those neurons that significantly participated to the calcium events within that particular cluster. Cell participation in a given cluster was considered statistically significant if the fraction of synchronous events in that cluster that activated the cell exceeded the 95th percentile of reshuffled data. If a neuron was significantly active in more than one cluster, it was associated to the one in which it participated the most (based on percentage). The overlap between assemblies/subnetworks was quantified by calculating the silhouette value of each cell (with the normalized hamming distance between each cell pair as a dissimilarity metric). A neuron was significantly involved in a single cluster if its silhouette value was higher than expected by chance (95th percentile after reshuffling). Calcium events were finally sorted with respect to their projection onto neuronal subnetworks. We computed the tetrachoric correlation coefficients for detected event (binary format) for all possible neuronal pairs or neuronal pairs within their subnetwork.

To test the robustness of the k-means clustering results, we compared our results to those obtained from two alternative similarity metrices: including cosine similarity and Jaccard similarity. We replaced the covariance matrix with the respective alternate values and complete the remaining steps of analyses identically. In addition to unsupervised k-means clustering algorithm, we also utilized semi-supervised Louvain community detection algorithm (Baum et al., 2016; Betzel et al., 2019; Rubinov and Sporns, 2010) to cluster the calcium event. Two commonly used models, the uniform null model (Bazzi et al., 2016) and the asymmetric model (Rubinov and Sporns, 2011), developed for the neuroscience field were chosen to cluster the covariance similarity matrix. Five hundred and 100 iterations were run for the uniform and asymmetric models followed with 10 iterations of consensus clustering without removing any weak elements (Lancichinetti and Fortunato, 2012). The iterations number were chosen based on clustering result reach converge. After the community detection algorithm identified the event cluster, we completed the remaining steps of analyses identically.

Immunohistochemistry, imaging, and quantification

Mice were anesthetized with isoflurane and perfused with 4% paraformaldehyde prepared in phosphate buffered saline (PBS) for ten minutes at a pump rate of ~2 mL/minute. Fixed brains were sectioned into 100 µm sections in the coronal plane using a Leica VT-1000 vibrating microtome (Leica Microsystems) and stored in antigen preserved solution (PBS, 50% ethylene glycol and 1% polyvinyl pyrrolidone) at -20 °C until later analysis. Sections were permeabilized with 2% Triton X100, then incubated with a blocking solution (3% normal goat serum prepared in PBS with 0.3% Triton X-100) and then incubated overnight with primary antibody prepared in blocking solution. An appropriate secondary antibody conjugated with an Alexa series fluorophore was used to detect the primary antibody. DAPI (100 ng/ml, Thermo Fisher) was included in the secondary antibody solution to stain nuclei. For imaging, Z-stack confocal images were acquired from both hemispheres with a Nikon A1 confocal microscope with a 10X/NA0.45 objective. The Z-stacks were taken at 1 µm intervals, and 5 µm-total thickness was imaged. To quantify the colocalization of different markers, single-plane images were used for visual inspection by using NIH ImageJ software.

Statistical analysis

The determination of statistical significance was performed using GraphPad Prism 9.4 software (GraphPad Software, San Diego, CA). Statistical details are found in supplementary tables associated with each figure and supplementary figure legends, including sample sizes, test, statistics, and p-values. Error is reported in figures as mean ± standard error of the mean (±SEM), unless otherwise noted.

Figure Supplementary 1. Imaging setting and calcium imaging data analysis workflow. (A) A stainless-steel armature surrounding the cranial window was affixed to the skull. (B)The metal bar is screwed onto the armature to provide anchoring points. (C) A photo of a P13 neonatal pup on the imaging station. A heating plate was embedded under the metal platform to keep the pup warm. The center of the lightweight foam disk covered by a circular piece of paper drape (blue) is fixed. The disk rotates as the pup walks, allowing free limb movement while the head remained fixed for imaging. (D) A bright-field image of the brain showing the place relative placement of the cranial glass window. The glass window was constructed by fastening together two cover glasses with diameters of 3 and 2.3 mm by optically transparent adhesive. (E) The dorsal view of brain tissue from a mouse with a window installed at P8 and perfused at P30. The imaging area is restricted to the upper right corner to target the somatosensory cortex. A, anterior; P, posterior; M, midline; L, lateral. (F) The data analysis workflow. (G) Exemplar figure includes detected calcium event, pup's body movement, and facial and whisker movement. This allowed us to choose a time for analysis when an animal had minimal body movement (stationary status). (H) Violin plot shows the distribution of accumulated summed calcium events of neurons in females and males over development. Kruskal-Wallis test. ***$p<0.001$. The mean correlation coefficients (I) and synchrony frequency (J) of L2/3 and L4 neurons from females and males from P11-P21. Three-way ANOVA main effect are stated in the figure.

Figure Supplementary 2. Additional clustering methods showed a similar developmental trajectory in silhouette value and the percentage of neurons in a single cluster. (A) The silhouette value of calcium event cluster, numbers of neuronal subnetwork, percentage of neurons not involved in any calcium event cluster, percentage of neurons participating in a single cluster, and percentage of neurons participating in multiple clusters. Three-way ANOVA main effect are stated in the figure. (B)The additional tree clustering methods. We performed the k-means clustering by using alternative similarity matrices (cosine similarity and Jaccard similarity) and covariance similarity matrix clustered by the Louvain community detection algorithm with either a uniform model or an asymmetric model. The additional three clustering methods showed a similar developmental trajectory in silhouette value and the percentage of neurons in a single cluster. Three-way ANOVA main effect are stated in the figure. The mean correlation coefficients of tetrachoric correlation coefficient from all neuronal pairs and neuronal pairs within the same subnetwork (D) of L2/3 and L4 neurons from females and males during P11-P21. Three-way ANOVA main effect are stated in the figure.

Figure Supplementary 3. (A) A representative calcium movie (maximum intensity projection across time) from a P15 mouse receiving AAV-carrying excitatory DREADD. The yellow dashed circles indicate neurons expressing nuclear Tomato red fluorescent protein that were excluded from data analysis during ROI curation. (B) Brain sections from a P21 mouse after calcium imaging. The white line indicates window placement. (C) A higher magnification image from the white dashed rectangle in B. I-VI, cortical layers. Brain sections were stained with CamK2 antibody (for glutamatergic neurons), anti-GFP antibody (for GABAergic neurons, the mouse is from a GAD67-GFP line), and DAPI for visualizing nuclei. (D) A higher magnification image from the yellow dashed rectangle in C. The signal for each channel was adjusted to best visualize the signal. D1 shows CamK2 positive neurons and GFP positive neurons, which were never colocalized. D2 shows that some of the jRGECO1a and nuclear Tom positive neurons also express GFP (yellow cells). D3-D6 each depict the single channel for each marker. Cells expressing jREGCO1a and nuclear Tom signals in nuclei (DAPI) are marked by a yellow dashed circle. These cells were not CamK2 positive neurons, but some were GFP positive neurons. (E) The percentage of GAD positive and CamK2 positive neurons in all jRGECO1 positive neurons. (F) The percentage of GAD positive and CamK2 positive neurons in nuclear Tom positive neurons.

References:

Alexander, G.M., Rogan, S.C., Abbas, A.I., Armbruster, B.N., Pei, Y., Allen, J.A., Nonneman, R.J., Hartmann, J., Moy, S.S., Nicolelis, M.A., et al. (2009). Remote control of neuronal activity in transgenic mice expressing evolved G protein-coupled receptors. Neuron *63*, 27-39. 10.1016/j.neuron.2009.06.014.

Arakawa, H., and Erzurumlu, R.S. (2015). Role of whiskers in sensorimotor development of C57BL/6 mice. Behav Brain Res *287*, 146-155. 10.1016/j.bbr.2015.03.040.

Ashby, M.C., and Isaac, J.T. (2011). Maturation of a recurrent excitatory neocortical circuit by experience-dependent unsilencing of newly formed dendritic spines. Neuron *70*, 510-521. 10.1016/j.neuron.2011.02.057.

Avitan, L., and Stringer, C. (2022). Not so spontaneous: Multi-dimensional representations of behaviors and context in sensory areas. Neuron. 10.1016/j.neuron.2022.06.019.

Baum, P., Vogt, M.A., Gass, P., Unsicker, K., and von Bohlen und Halbach, O. (2016). FGF-2 deficiency causes dysregulation of Arhgef6 and downstream targets in the cerebral cortex accompanied by altered neurite outgrowth and dendritic spine morphology. Int J Dev Neurosci *50*, 55-64. 10.1016/j.ijdevneu.2016.03.002.

Bazzi, M., Porter, M.A., Williams, S., McDonald, M., Fenn, D.J., and Howison, S.D. (2016). Community Detection in Temporal Multilayer Networks, with an Application to Correlation Networks. Multiscale Modeling & Simulation *14*, 1-41. 10.1137/15m1009615.

Betzel, R.F., Wood, K.C., Angeloni, C., Neimark Geffen, M., and Bassett, D.S. (2019). Stability of spontaneous, correlated activity in mouse auditory cortex. PLoS Comput Biol *15*, e1007360. 10.1371/journal.pcbi.1007360.

Buzsaki, G. (2010). Neural syntax: cell assemblies, synapsembles, and readers. Neuron *68*, 362-385. 10.1016/j.neuron.2010.09.023.

Carrillo-Reid, L., Yang, W., Bando, Y., Peterka, D.S., and Yuste, R. (2016). Imprinting and recalling cortical ensembles. Science *353*, 691-694. 10.1126/science.aaf7560.

Clavreul, S., Abdeladim, L., Hernandez-Garzon, E., Niculescu, D., Durand, J., Ieng, S.H., Barry, R., Bonvento, G., Beaurepaire, E., Livet, J., and Loulier, K. (2019). Cortical astrocytes develop in a plastic manner at both clonal and cellular levels. Nat Commun *10*, 4884. 10.1038/s41467-019-12791-5.

Cossell, L., Iacaruso, M.F., Muir, D.R., Houlton, R., Sader, E.N., Ko, H., Hofer, S.B., and Mrsic-Flogel, T.D. (2015). Functional organization of excitatory synaptic strength in primary visual cortex. Nature *518*, 399-403. 10.1038/nature14182.

Dana, H., Mohar, B., Sun, Y., Narayan, S., Gordus, A., Hasseman, J.P., Tsegaye, G., Holt, G.T., Hu, A., Walpita, D., et al. (2016). Sensitive red protein calcium indicators for imaging neural activity. Elife *5*. 10.7554/eLife.12727.

Daw, M.I., Ashby, M.C., and Isaac, J.T. (2007). Coordinated developmental recruitment of latent fast spiking interneurons in layer IV barrel cortex. Nat Neurosci *10*, 453-461. 10.1038/nn1866.

Dimidschstein, J., Chen, Q., Tremblay, R., Rogers, S.L., Saldi, G.A., Guo, L., Xu, Q., Liu, R., Lu, C., Chu, J., et al. (2016). A viral strategy for targeting and manipulating interneurons across vertebrate species. Nat Neurosci *19*, 1743-1749. 10.1038/nn.4430.

Dorn, J.D., and Ringach, D.L. (2003). Estimating membrane voltage correlations from extracellular spike trains. J Neurophysiol *89*, 2271-2278. 10.1152/jn.000889.2002.

Ferezou, I., and Deneux, T. (2017). Review: How do spontaneous and sensory-evoked activities interact? Neurophotonics *4*, 031221. 10.1117/1.NPh.4.3.031221.

Gerasimov, E., Erofeev, A., Borodinova, A., Bolshakova, A., Balaban, P., Bezprozvanny, I., and Vlasova, O.L. (2021). Optogenetic Activation of Astrocytes-Effects on Neuronal Network Function. Int J Mol Sci *22*. 10.3390/ijms22179613.

Goel, A., Cantu, D.A., Guilfoyle, J., Chaudhari, G.R., Newadkar, A., Todisco, B., de Alba, D., Kourdougli, N., Schmitt, L.M., Pedapati, E., et al. (2018). Impaired perceptual learning in a mouse model of Fragile X syndrome is mediated by parvalbumin neuron dysfunction and is reversible. Nat Neurosci *21*, 1404-1411. 10.1038/s41593-018-0231-0.
Golshani, P., Goncalves, J.T., Khoshkhoo, S., Mostany, R., Smirnakis, S., and Portera-Cailliau, C. (2009). Internally mediated developmental desynchronization of neocortical network activity. J Neurosci *29*, 10890-10899. 10.1523/JNEUROSCI.2012-09.2009.
Goncalves, J.T., Anstey, J.E., Golshani, P., and Portera-Cailliau, C. (2013). Circuit level defects in the developing neocortex of Fragile X mice. Nat Neurosci *16*, 903-909. 10.1038/nn.3415.
Gour, A., Boergens, K.M., Heike, N., Hua, Y., Laserstein, P., Song, K., and Helmstaedter, M. (2021). Postnatal connectomic development of inhibition in mouse barrel cortex. Science *371*. 10.1126/science.abb4534.
Haider, B., Duque, A., Hasenstaub, A.R., and McCormick, D.A. (2006). Neocortical network activity in vivo is generated through a dynamic balance of excitation and inhibition. J Neurosci *26*, 4535-4545. 10.1523/JNEUROSCI.5297-05.2006.
Harris, K.D., and Mrsic-Flogel, T.D. (2013). Cortical connectivity and sensory coding. Nature *503*, 51-58. 10.1038/nature12654.
Hartmann, C., Lazar, A., Nessler, B., and Triesch, J. (2015). Where's the Noise? Key Features of Spontaneous Activity and Neural Variability Arise through Learning in a Deterministic Network. PLoS Comput Biol *11*, e1004640. 10.1371/journal.pcbi.1004640.
He, C.X., Arroyo, E.D., Cantu, D.A., Goel, A., and Portera-Cailliau, C. (2018). A Versatile Method for Viral Transfection of Calcium Indicators in the Neonatal Mouse Brain. Front Neural Circuits *12*, 56. 10.3389/fncir.2018.00056.
He, C.X., Cantu, D.A., Mantri, S.S., Zeiger, W.A., Goel, A., and Portera-Cailliau, C. (2017). Tactile Defensiveness and Impaired Adaptation of Neuronal Activity in the Fmr1 Knock-Out Mouse Model of Autism. J Neurosci *37*, 6475-6487. 10.1523/JNEUROSCI.0651-17.2017.
Itami, C., Kimura, F., and Nakamura, S. (2007). Brain-derived neurotrophic factor regulates the maturation of layer 4 fast-spiking cells after the second postnatal week in the developing barrel cortex. J Neurosci *27*, 2241-2252. 10.1523/JNEUROSCI.3345-06.2007.
Kalemaki, K., Velli, A., Christodoulou, O., Denaxa, M., Karagogeos, D., and Sidiropoulou, K. (2022). The developmental changes in intrinsic and synaptic properties of prefrontal neurons enhance local network activity from the second to the third postnatal weeks in mice. Cereb Cortex *32*, 3633-3650. 10.1093/cercor/bhab438.
Karvat, G., Alyahyay, M., and Diester, I. (2021). Spontaneous activity competes with externally evoked responses in sensory cortex. Proc Natl Acad Sci U S A *118*. 10.1073/pnas.2023286118.
Keemink, S.W., Lowe, S.C., Pakan, J.M.P., Dylda, E., van Rossum, M.C.W., and Rochefort, N.L. (2018). FISSA: A neuropil decontamination toolbox for calcium imaging signals. Sci Rep *8*, 3493. 10.1038/s41598-018-21640-2.
Lancichinetti, A., and Fortunato, S. (2012). Consensus clustering in complex networks. Sci Rep *2*, 336. 10.1038/srep00336.
Lee, W.C., Bonin, V., Reed, M., Graham, B.J., Hood, G., Glattfelder, K., and Reid, R.C. (2016). Anatomy and function of an excitatory network in the visual cortex. Nature *532*, 370-374. 10.1038/nature17192.
Malvache, A., Reichinnek, S., Villette, V., Haimerl, C., and Cossart, R. (2016). Awake hippocampal reactivations project onto orthogonal neuronal assemblies. Science *353*, 1280-1283. 10.1126/science.aaf3319.
Mathis, A., Mamidanna, P., Cury, K.M., Abe, T., Murthy, V.N., Mathis, M.W., and Bethge, M. (2018). DeepLabCut: markerless pose estimation of user-defined body parts with deep learning. Nat Neurosci *21*, 1281-1289. 10.1038/s41593-018-0209-y.

Miller, J.E., Ayzenshtat, I., Carrillo-Reid, L., and Yuste, R. (2014). Visual stimuli recruit intrinsically generated cortical ensembles. Proc Natl Acad Sci U S A *111*, E4053-4061. 10.1073/pnas.1406077111.
Mizuno, H., Ikezoe, K., Nakazawa, S., Sato, T., Kitamura, K., and Iwasato, T. (2018). Patchwork-Type Spontaneous Activity in Neonatal Barrel Cortex Layer 4 Transmitted via Thalamocortical Projections. Cell Rep *22*, 123-135. 10.1016/j.celrep.2017.12.012.
Modol, L., Bollmann, Y., Tressard, T., Baude, A., Che, A., Duan, Z.R.S., Babij, R., De Marco Garcia, N.V., and Cossart, R. (2020). Assemblies of Perisomatic GABAergic Neurons in the Developing Barrel Cortex. Neuron *105*, 93-105 e104. 10.1016/j.neuron.2019.10.007.
Nakazawa, S., Yoshimura, Y., Takagi, M., Mizuno, H., and Iwasato, T. (2020). Developmental Phase Transitions in Spatial Organization of Spontaneous Activity in Postnatal Barrel Cortex Layer 4. J Neurosci *40*, 7637-7650. 10.1523/JNEUROSCI.1116-20.2020.
Nath, T., Mathis, A., Chen, A.C., Patel, A., Bethge, M., and Mathis, M.W. (2019). Using DeepLabCut for 3D markerless pose estimation across species and behaviors. Nat Protoc *14*, 2152-2176. 10.1038/s41596-019-0176-0.
Pachitariu, M., Stringer, C., Dipoppa, M., Schröder, S., Rossi, L.F., Dalgleish, H., Carandini, M., and Harris, K.D. (2017). Suite2p: beyond 10,000 neurons with standard two-photon microscopy. BioRxiv.
Peron, S., Pancholi, R., Voelcker, B., Wittenbach, J.D., Olafsdottir, H.F., Freeman, J., and Svoboda, K. (2020). Recurrent interactions in local cortical circuits. Nature *579*, 256-259. 10.1038/s41586-020-2062-x.
Peron, S.P., Freeman, J., Iyer, V., Guo, C., and Svoboda, K. (2015). A Cellular Resolution Map of Barrel Cortex Activity during Tactile Behavior. Neuron *86*, 783-799. 10.1016/j.neuron.2015.03.027.
Rubinov, M., and Sporns, O. (2010). Complex network measures of brain connectivity: uses and interpretations. Neuroimage *52*, 1059-1069. 10.1016/j.neuroimage.2009.10.003.
Rubinov, M., and Sporns, O. (2011). Weight-conserving characterization of complex functional brain networks. Neuroimage *56*, 2068-2079. 10.1016/j.neuroimage.2011.03.069.
Rurak, G.M., Simard, S., Freitas-Andrade, M., Lacoste, B., Charih, F., Van Geel, A., Stead, J., Woodside, B., Green, J.R., Coppola, G., and Salmaso, N. (2022). Sex differences in developmental patterns of neocortical astroglia: A mouse translatome database. Cell Rep *38*, 110310. 10.1016/j.celrep.2022.110310.
Schindelin, J., Arganda-Carreras, I., Frise, E., Kaynig, V., Longair, M., Pietzsch, T., Preibisch, S., Rueden, C., Saalfeld, S., Schmid, B., et al. (2012). Fiji: an open-source platform for biological-image analysis. Nat Methods *9*, 676-682. 10.1038/nmeth.2019.
Shu, Y., Hasenstaub, A., and McCormick, D.A. (2003). Turning on and off recurrent balanced cortical activity. Nature *423*, 288-293. 10.1038/nature01616.
Sigalas, C., Konsolaki, E., and Skaliora, I. (2017). Sex differences in endogenous cortical network activity: spontaneously recurring Up/Down states. Biol Sex Differ *8*, 21. 10.1186/s13293-017-0143-9.
Stogsdill, J.A., Ramirez, J., Liu, D., Kim, Y.H., Baldwin, K.T., Enustun, E., Ejikeme, T., Ji, R.R., and Eroglu, C. (2017). Astrocytic neuroligins control astrocyte morphogenesis and synaptogenesis. Nature *551*, 192-197. 10.1038/nature24638.
Stringer, C., Pachitariu, M., Steinmetz, N., Reddy, C.B., Carandini, M., and Harris, K.D. (2019). Spontaneous behaviors drive multidimensional, brainwide activity. Science *364*, 255. 10.1126/science.aav7893.
Tamamaki, N., Yanagawa, Y., Tomioka, R., Miyazaki, J., Obata, K., and Kaneko, T. (2003). Green fluorescent protein expression and colocalization with calretinin, parvalbumin, and somatostatin in the GAD67-GFP knock-in mouse. J Comp Neurol *467*, 60-79. 10.1002/cne.10905.
Thompson, A., Gribizis, A., Chen, C., and Crair, M.C. (2017). Activity-dependent development of visual receptive fields. Curr Opin Neurobiol *42*, 136-143. 10.1016/j.conb.2016.12.007.

Towns, J., Cockerill, T., Dahan, M., Foster, I., Gaither, K., Grimshaw, A., Hazlewood, V., Lathrop, S., Lifka, D., Peterson, G.D., et al. (2014). XSEDE: Accelerating Scientific Discovery. Comput Sci Eng *16*, 62-74. Doi 10.1109/Mcse.2014.80.
Valiullina, F., Akhmetshina, D., Nasretdinov, A., Mukhtarov, M., Valeeva, G., Khazipov, R., and Rozov, A. (2016). Developmental Changes in Electrophysiological Properties and a Transition from Electrical to Chemical Coupling between Excitatory Layer 4 Neurons in the Rat Barrel Cortex. Front Neural Circuits *10*, 1. 10.3389/fncir.2016.00001.
Van Den Herrewegen, Y., Sanderson, T.M., Sahu, S., De Bundel, D., Bortolotto, Z.A., and Smolders, I. (2021). Side-by-side comparison of the effects of Gq- and Gi-DREADD-mediated astrocyte modulation on intracellular calcium dynamics and synaptic plasticity in the hippocampal CA1. Mol Brain *14*, 144. 10.1186/s13041-021-00856-w.
van der Bourg, A., Yang, J.W., Reyes-Puerta, V., Laurenczy, B., Wieckhorst, M., Stuttgen, M.C., Luhmann, H.J., and Helmchen, F. (2017). Layer-Specific Refinement of Sensory Coding in Developing Mouse Barrel Cortex. Cereb Cortex *27*, 4835-4850. 10.1093/cercor/bhw280.
Yassin, L., Benedetti, B.L., Jouhanneau, J.S., Wen, J.A., Poulet, J.F., and Barth, A.L. (2010). An embedded subnetwork of highly active neurons in the neocortex. Neuron *68*, 1043-1050. 10.1016/j.neuron.2010.11.029.
Yoshimura, Y., Dantzker, J.L., and Callaway, E.M. (2005). Excitatory cortical neurons form fine-scale functional networks. Nature *433*, 868-873. 10.1038/nature03252.
Yu, J., Hu, H., Agmon, A., and Svoboda, K. (2019). Recruitment of GABAergic Interneurons in the Barrel Cortex during Active Tactile Behavior. Neuron *104*, 412-427 e414. 10.1016/j.neuron.2019.07.027.

Figure 1

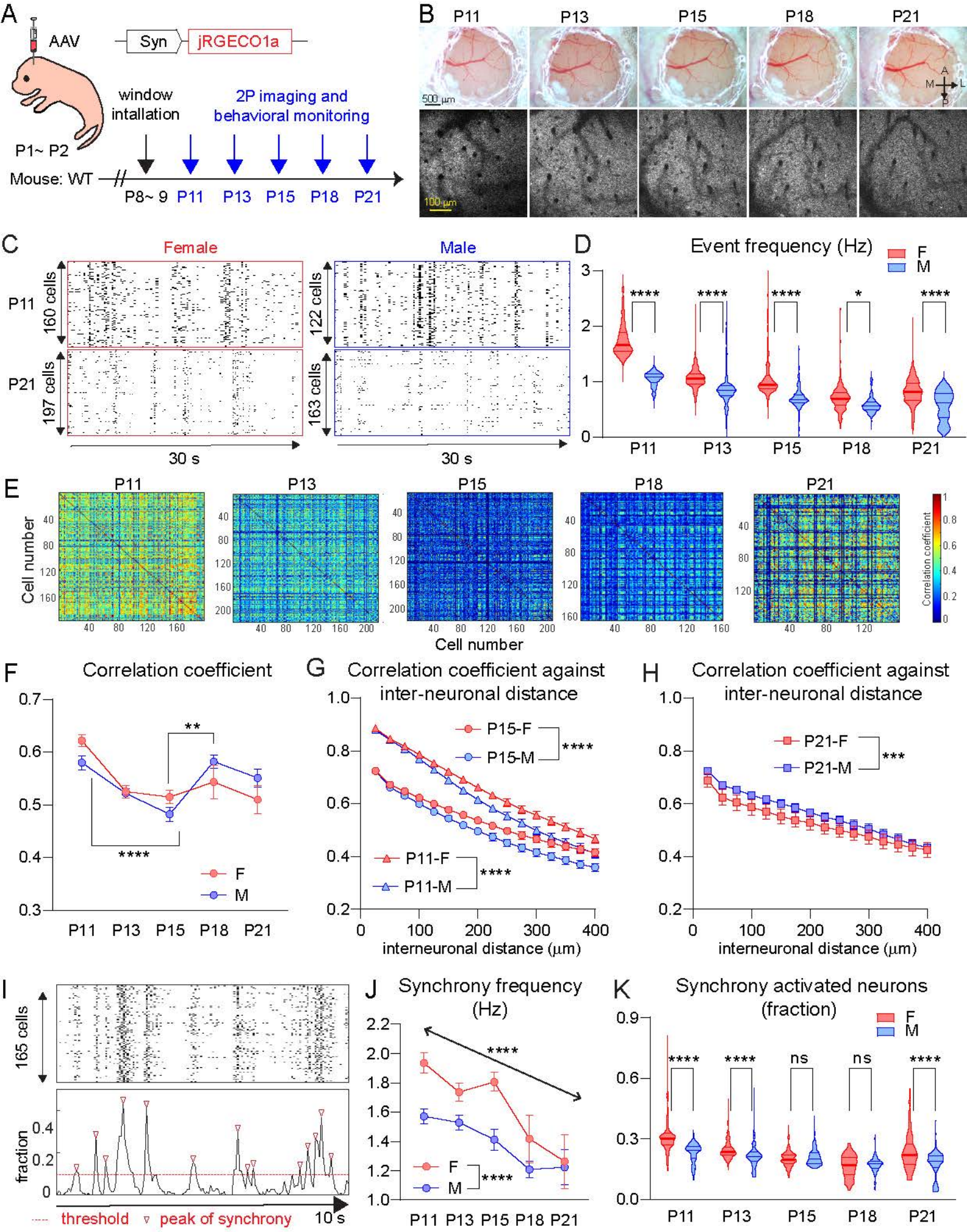
A
AAV
Syn
jRGECO1a
window intallation
2P imaging and behavioral monitoring
P1~ P2
Mouse: WT
P8~ 9
P11
P13
P15
P18
P21
B
500 μm
100 μm
C
Female
Male
160 cells
197 cells
122 cells
163 cells
30 s
D
Event frequency (Hz)
F
M
E
Cell number
Correlation coefficient
F
Correlation coefficient
G
Correlation coefficient against inter-neuronal distance
P15-F
P15-M
P11-F
P11-M
interneuronal distance (μm)
H
Correlation coefficient against inter-neuronal distance
P21-F
P21-M
I
165 cells
fraction
threshold
peak of synchrony
10 s
J
Synchrony frequency (Hz)
K
Synchrony activated neurons (fraction)
ns

Figure 2

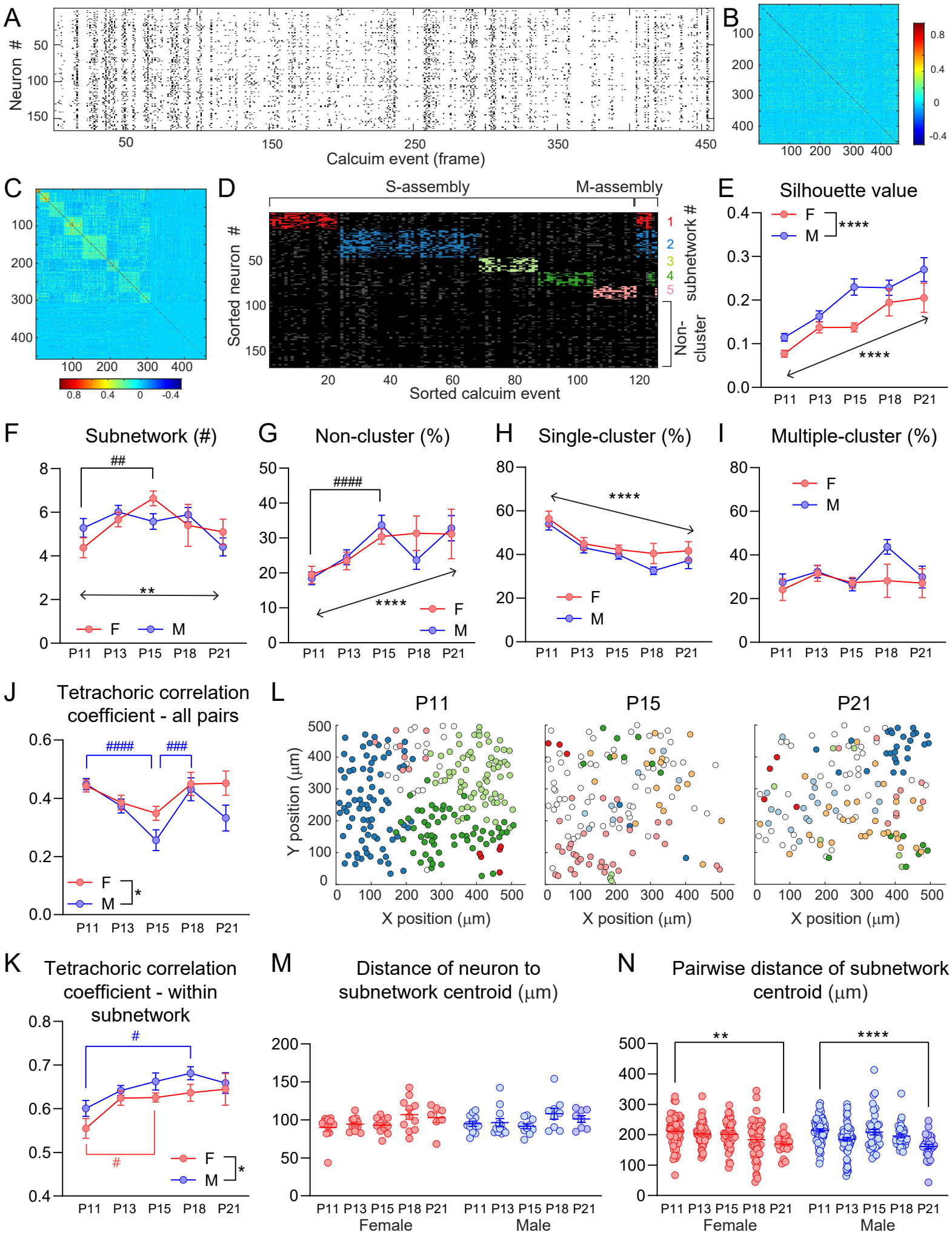
A
Neuron #
Calcuim event (frame)
B
C
D
S-assembly
M-assembly
Sorted neuron #
Sorted calcuim event
subnetwork #
Non-cluster
E
Silhouette value
F
M
****
P11 P13 P15 P18 P21
F
Subnetwork (#)
##
**
G
Non-cluster (%)
####
****
H
Single-cluster (%)
I
Multiple-cluster (%)
J
Tetrachoric correlation coefficient - all pairs
####
###
*
L
P11
P15
P21
Y position (μm)
X position (μm)
K
Tetrachoric correlation coefficient - within subnetwork
#
M
Distance of neuron to subnetwork centroid (μm)
Female
Male
N
Pairwise distance of subnetwork centroid (μm)
**
****

Figure 3

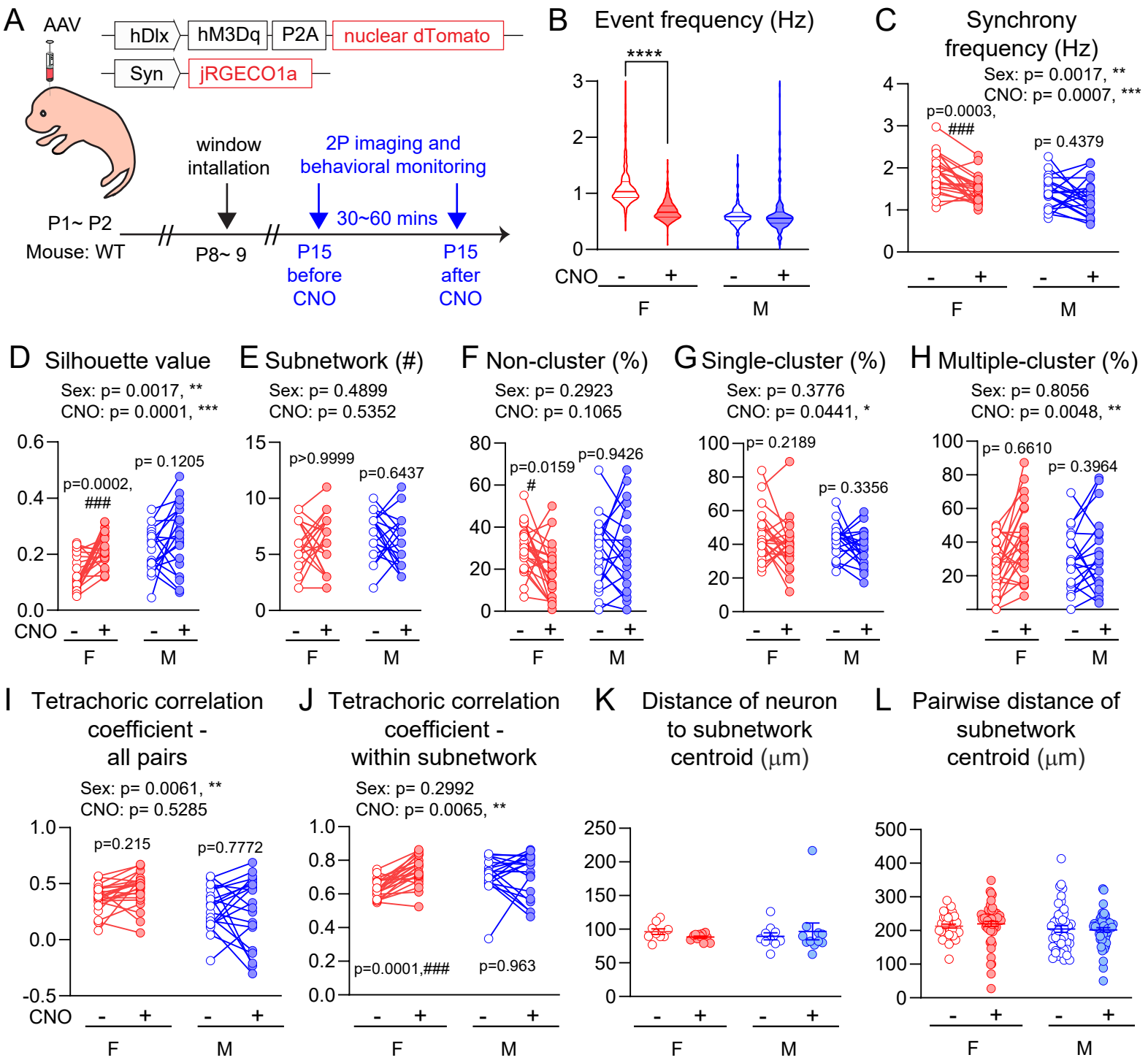
A
AAV
hDlx
hM3Dq
P2A
nuclear dTomato
Syn
jRGECO1a
window intallation
2P imaging and behavioral monitoring
30~60 mins
P1~ P2
Mouse: WT
P8~ 9
P15 before CNO
P15 after CNO
B
Event frequency (Hz)
****
CNO
F
M
C
Synchrony frequency (Hz)
Sex: p= 0.0017, **
CNO: p= 0.0007, ***
p=0.0003, ###
p= 0.4379
D
Silhouette value
Sex: p= 0.0017, **
CNO: p= 0.0001, ***
p=0.0002, ###
p= 0.1205
E
Subnetwork (#)
Sex: p= 0.4899
CNO: p= 0.5352
p>0.9999
p=0.6437
F
Non-cluster (%)
Sex: p= 0.2923
CNO: p= 0.1065
p=0.0159 #
p=0.9426
G
Single-cluster (%)
Sex: p= 0.3776
CNO: p= 0.0441, *
p= 0.2189
p= 0.3356
H
Multiple-cluster (%)
Sex: p= 0.8056
CNO: p= 0.0048, **
p= 0.6610
p= 0.3964
I
Tetrachoric correlation coefficient - all pairs
Sex: p= 0.0061, **
CNO: p= 0.5285
p=0.215
p=0.7772
J
Tetrachoric correlation coefficient - within subnetwork
Sex: p= 0.2992
CNO: p= 0.0065, **
p=0.0001,###
p=0.963
K
Distance of neuron to subnetwork centroid (μm)
L
Pairwise distance of subnetwork centroid (μm)

Supp Figure 1

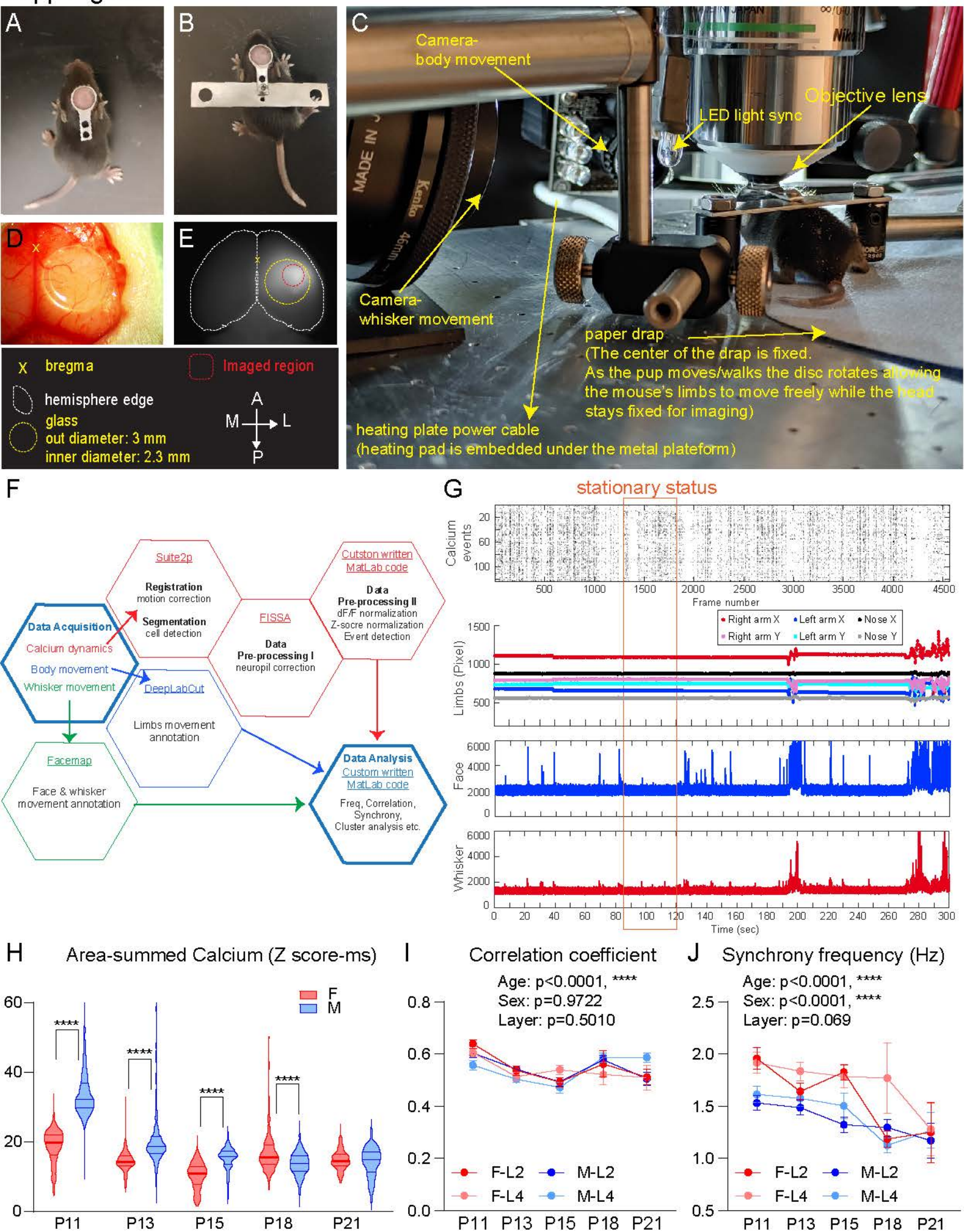

Supp Figure 2

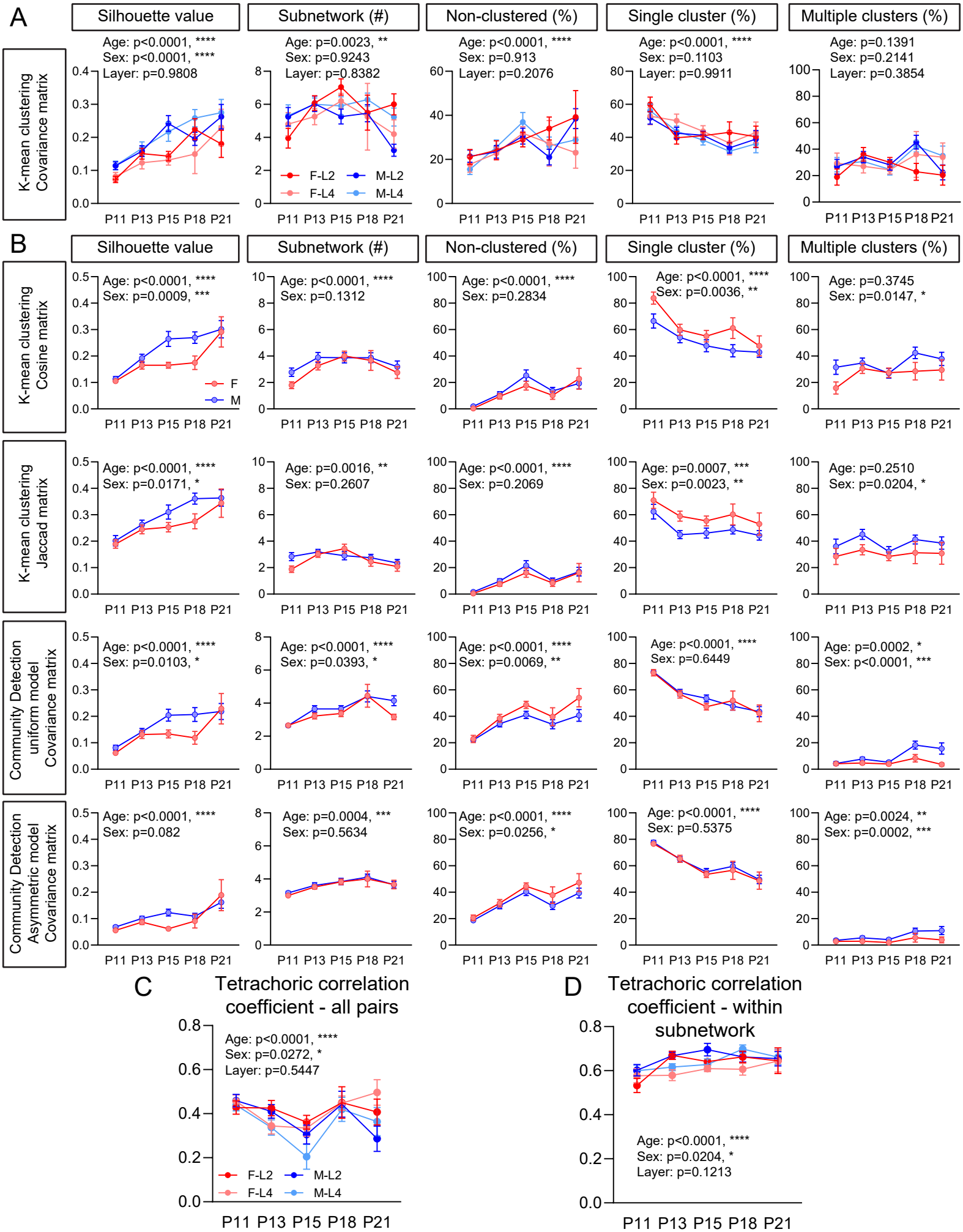
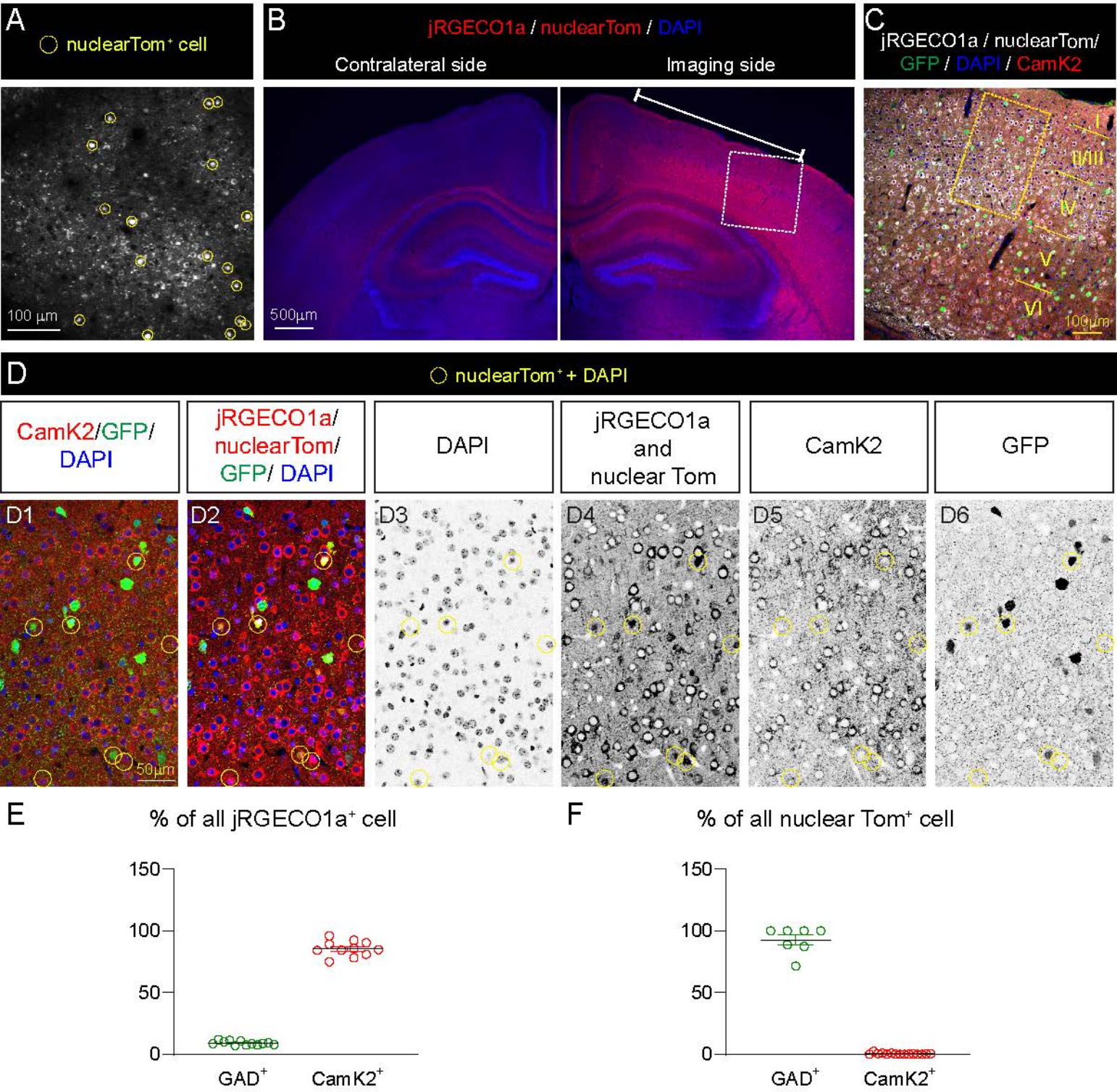
Supp Figure 3